2019

Phase separation and enhanced wear resistance of Cu88Fe12 immiscible coating prepared by laser cladding

Shuzhen Zhao

Shengfeng Zhou

Min Xie

Xiaoqin Dai

Dongchu Chen

See next page for additional authors

10.1016/j.jmrt.2018.12.018

Zhao, S., Zhou, S., Xie, M., Dai, X., Chen, D., & Zhang, L. (2019). Phase separation and enhanced wear resistance of Cu88Fe12 immiscible coating prepared by laser cladding. *Journal of Materials Research and Technology*, *8*(2), 2001-2010. Available here

Available online at www.sciencedirect.com

jmr&t Journal of Materials Research and Technology

www.jmrt.com.br

Original Article

Phase separation and enhanced wear resistance of Cu88Fe12 immiscible coating prepared by laser cladding

Shuzhen Zhao[a], *Shengfeng Zhou*[a,*], *Min Xie*[a], *Xiaoqin Dai*[a,*], *Dongchu Chen*[b,*], *Lai-Chang Zhang*[c,*]

[a] *Laser Technology Institute, Tianjin Polytechnic University, Tianjin, 300387, China*
[b] *School of Materials Science and Energy Engineering, Foshan University, Foshan, Guangdong, 52800, China*
[c] *School of Engineering, Edith Cowan University, 270 Joondalup Drive, Joondalup, Perth, WA 6027, Australia*

ARTICLE INFO

Article history:
Received 7 July 2018
Accepted 21 December 2018
Available online 18 March 2019

Keywords:
Immiscible alloy
Cu–Fe
Liquid phase separation
Microstructure
Wear resistance

ABSTRACT

In order to eliminate the microstructure segregation of Cu–Fe immiscible alloys which characterized with a liquid miscible gap, the Cu88Fe12 (wt.%) immiscible coating was prepared by laser cladding. The phase separation characteristic and wear resistance of the Cu88Fe12 (wt.%) immiscible coating were also investigated. The results show that the size of the milled Cu88Fe12 composite powder is reduced comparing to that of the un-milled powder due to fracturing during mechanical milling. Moreover, the demixing or delamination disappears in the Cu88Fe12 immiscible coating and a large amount of face-centered-cubic (fcc) γ-Fe and body-centered-cubic (bcc) α-Fe particles are dispersed in the face-centered-cubic (fcc) ε-Cu matrix as a result of liquid phase separation. The size of Fe-rich particles presents an increasing tendency from the bottom to the top of the immiscible coating. As a result, the microhardness of the immiscible coating is improved compared with brass (~138 $HV_{0.2}$) due to the presence of high-hardness Fe-rich particles (~191 $HV_{0.2}$) and the solid solution strengthening effect of Fe in Cu-rich matrix. Furthermore, the width of ploughing, the width and height of wear scar on the surface of the immiscible coating are much less than those on the surface of brass. Therefore, the wear resistance of the immiscible coating is remarkably enhanced compared with brass.

* *Corresponding authors.*
E-mails: zhousf1228@163.com (S. Zhou), daixq0827@163.com (X. Dai), chendc@fosu.edu.cn (D. Chen), l.zhang@ecu.edu.au, lczhangimr@gmail.com (L. Zhang).
https://doi.org/10.1016/j.jmrt.2018.12.018

1. Introduction

Immiscible alloys, whether it is binary or ternary alloy, such as Al–Bi/In [1], Cu–Co/Cu–Co–Fe [2–5], Cu–Nb [6], Ag–Cu [7], Fe–Ag [8], Cu–Fe–Ag/Cr [9], Fe–Cu [10,11], which have a common characteristic, a metastable liquid immiscible gap. When they are supercooled and entered the metastable liquid immiscible gap, liquid phase separation which can be described as the single melt can separate into two melts occurs inevitably. Subsequently, if the acquired microstructure is characterized by the minor phase dispersed within the major matrix or core–shell structure [12,13], the immiscible alloys can exhibit a variety of excellent performances, such as self-lubrication, giant magnetoresistance (GMR), high superconductivity, high strength, high conductively and excellent soft magnetic performance. Therefore, the immiscible alloys can be used for self-lubrication bearing materials, electrical contact materials, pulsed high-field magnets, optical devices, sensors, magnetic recording and packaging materials [1,9–14].

However, the macroscopic segregation is easy to occur during solidification due to the difference in two liquid phases densities, which has limited the scope of potential application. To overcome this defect, a considerable amount of methods, have been proposed continuously to obtain the desired immiscible alloys with uniform microstructure, such as electromagnetic levitation and drop tube [15,16]. For example, Cao et al. [17] produced the Cu68Co32 (at.%) immiscible alloys by electromagnetic levitation and found that the spherical Co-rich particles can distributed nearly homogeneously within the Cu-rich matrix, which is due to the fact that in the electromagnetic levitation process, the electromagnetic stirring can weaken macroscopic coagulation among different Co-rich droplets. Moreover, Cao et al. [18] produced the Co–40 wt.% Cu immiscible alloys by drop tube and found that uniform dispersion could be formed in small droplets, whereas small-scale inhomogeneities near the surface existed in large droplets. Obviously, although heterogeneous nucleation and microgravity induced segregation can be inhibited to some extent, the serious segregation exists in the immiscible alloys.

Recently, the rapid solidification techniques, such as gas atomization, melt spinning and laser cladding, whose cooling rate can reach 10^5–10^7 K/s have potential advantages in fabricating the immiscible alloys with desired homogeneous microstructure [2]. Wang et al. [13,19] produced the Cu–Fe immiscible alloy powders with egg-type microstructure where one alloy encases another by gas atomization. Nagase et al. [20] produced the binary Fe–Cu and ternary Fe–Cu–B immiscible alloys by melt spinning and found that the duplex structure composed of Fe–B-rich and Cu-rich alloys was formed as a result of liquid phase separation regardless of the B content. Zhou et al. [21] also reported that the duplex composite coatings composed of a Cu-rich particle (Cu_p)-reinforced Fe-rich layer and Fe-rich particles (Fe_p)-reinforced Cu-rich layer were synthesized in situ by laser cladding, and found that the addition of Si resulted in the coarsening of Cu-rich and Fe-rich particles.

Moreover, our previous studies reported the effect of processing parameters on the phase separation characteristics and properties of Cu–Fe immiscible coatings prepared by laser induction hybrid cladding (LIHC). For instance, the uniform distribution of CNTs-Fe_p resulted in an increase in thermal conductively, hardness and wear resistance of Cu–Fe immiscible alloys [22]. The increasing of Al (0–10 wt.%) caused the Fe-rich particles to grow up, the higher of the Cu-rich grains precipitated inside the Fe-rich particles and the better of the electrochemical corrosion resistance of Cu–Fe–C immiscible alloys [23]. The Cu_p/Fe–Fe_p/Cu duplex-layer structure and the Fe_p/Cu–Cu_p/Fe–Fe_p/Cu sandwich-layer structure can be formed on Fe-substrate and Cu-substrate, respectively [24]. The increasing of laser scanning speed could decrease the temperature of the molten pool and increase the cooling rate of the molten pool, leading to a reduction in size of Fe- and Cu-rich particles of the Cu35(FeCrC)65 (wt.%) immiscible alloys [25]. However, the demixing or delamination phenomenon still exists in the Cu–Fe immiscible coatings produced by LIHC.

In order to eliminate the demixing or delamination phenomenon, Dai et al. [26] adopted the combination of mechanical alloying and laser cladding to prepared the Cu95Fe5 (wt.%) homogeneous immiscible coating with an enhanced corrosion resistance, a saturated magnetization of ~9.19 emu/g and a low coercivity of ~9.25 Oe, but the wear resistance of the immiscible coating is not still dealt with. In the present work. According to the Cu–Fe phase diagram, the element composition is designed [26] and the Cu88Fe12 (wt.%) homogeneous immiscible coating without demixing or delamination is successfully prepared by laser cladding. The emphasis of the present paper is to investigate the phase separation characteristics and wear behavior of Cu88Fe12 immiscible coating.

2. Experimental

Low carbon steel with the dimension of 100 mm × 50 mm × 10 mm was used as the substrate. The Cu–Fe alloy powder was composed of 88 wt.% pure copper powder (99.5% purity) and 12 wt.% Fe–12Ni–5Cr–0.6Si–0.2 C powder. Before laser cladding, the Cu88Fe12 (wt.%) composite powder was mechanically milled at the rate of 200 rpm in a planetary ball milling for 16 h. The milling time was set as an on/off cycle of 30 min and 15 min in order to avoid temperature rise during mechanical alloying. The weight ratio of ball to powder was set as 15:1 and the stainless balls with different diameters were used as grinding materials. Finally, the milled composite powder was put into an electric furnace at 120 °C for 3 h and then was used as cladding material.

The cladding material with a thickness of ~2 mm was replaced on the surface of substrate, and then laser cladding was performed by a semiconductor laser with a wavelength of 800 nm to produce the Cu88Fe12 immiscible coating. High purity Ar gas was used as shielding gas to be blown into the molten pool. The optimal processing parameters were adopted as follows: laser power 2 kW, spot size 8 mm × 4 mm and laser scanning speed used 8 mm/s.

The immiscible coating was etched by a solution composed of 5 g $FeCl_3$ (99.9% purity), 5 ml HCl (37 wt.% Analytical reagent) and 95 ml H_2O for 15 s. Microstructure was observed by a PHILIP-XL30 scanning electron microscope (SEM) equipped with energy dispersive spectroscopy (EDS). Phase constituents

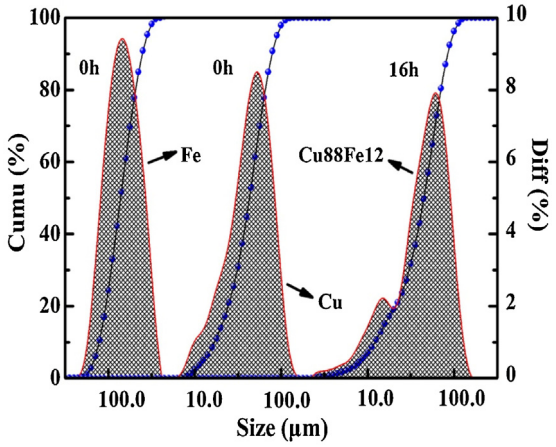

Fig. 1 – The size distribution of primary un-milled powder and milled composite powder.

were identified by D/MAX-2500 X-ray diffractometer (XRD, Cu target, 40 kV and 40 mA).

An HV-1000 Vickers microhardness tester with a load of 1.96 N and a hold time of 10 s was used to evaluate the hardness of the Cu–Fe immiscible coating and brass. Moreover, the images of microhardness indentation were also observed by SEM. The dry sliding wear were conducted by using a block-on-ring M-2000 wear machine with a load of 50 N and a sliding speed of 200 rpm for 120 min at room temperature. The size of the block was 6.5 mm × 6.5 mm × 8 mm and the counterpart ring (50 mm in external diameter) was made from the hardened GCr15 steel with a hardness of 60 HRC. The friction coefficient could be obtained during dry sliding wear and the weight losses were recorded by an electronic balance with a sensitivity of 0.1 mg. After dry sliding wear, the morphologies of wear debris and the worn surfaces were analyzed by SEM and EDS. The depth and width of the wear track were also observed by Phase Shift MicroXAM-3D.

3. Results and discussion

3.1. *Microstructure characteristics of immiscible coating*

Fig. 1 shows the size distribution of un-milled and milled composite powder. The sizes of primary Fe-based powder and pure Cu powder (D50) are ~128 μm and ~48 μm, respectively. However, the size of milled composite powder (D50) is reduced to ~29 μm, indicating that fracturing occurs during mechanical milling.

Fig. 2 shows the XRD patterns of the primary Cu and Fe powders and the Cu88Fe12 immiscible coating. The diffraction angles of Cu powder corresponding to the diffraction peaks (111), (200), (220) are 43.3°, 50.5°, 74.2°, respectively, while the diffraction angles of Fe powder corresponding to the diffraction peaks (111), (110), (200), (220) are 42.9°, 44.7°, 50.0°, 73.3°, respectively (Fig. 2a). As can be seen, there is slight difference in diffraction peaks between the primary pure Cu powder and Fe powder. Moreover, the overlapping diffraction peaks (111), (200), (220) of ε-Cu and γ-Fe can be observed and the

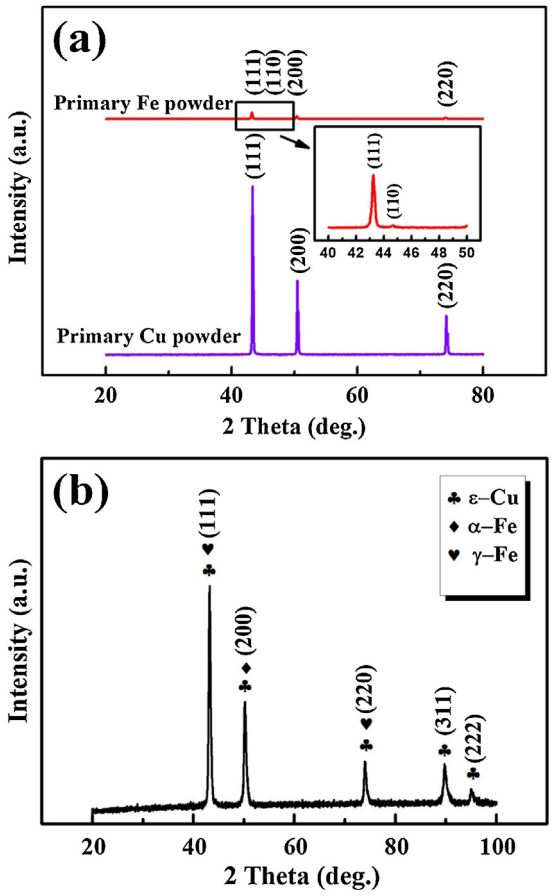

Fig. 2 – (a) The XRD patterns of primary Fe and Cu powders and (b) Cu88Fe12 immiscible coating.

Table 1 – The EDS results of microstructure in the immiscible coating shown in Fig.3.

Microstructure	Composition (wt.%)			
	Cu	Fe	Cr	Ni
I	16.8	57.2	8.2	17.8
II	85.0	9.1	–	5.9

intensity of diffraction peak (110) of α-Fe is very weak in the immiscible coating. Generally, the solid solubility of Fe in ε-Cu and that of Cu in γ/α-Fe can be negligible under the condition of equilibrium solidification [4,21]. However, the solid solubility of Fe in Cu and that of Cu in Fe increase substantially during LC due to rapid solidification, resulting in the formation of face-centered-cubic (fcc) ε-Cu matrix containing a supersaturated Fe, face-centered-cubic (fcc) γ-Fe and body-centered-cubic (bcc) α-Fe particles containing a supersaturated Cu (Table 1). As a result, the diffraction peaks of ε-Cu are widened and those of γ-Fe are shifted (Fig. 2b).

Fig. 3 illustrates the cross-sectional morphologies of Cu88Fe12 immiscible coating. It is noted that the demixing of microstructure does not appear in the immiscible coating, which is similar to the previous study on the homogeneous microstructure of the Cu95Fe5 immiscible coating by the combination of mechanical milling and laser cladding [26]. Fig. 3a

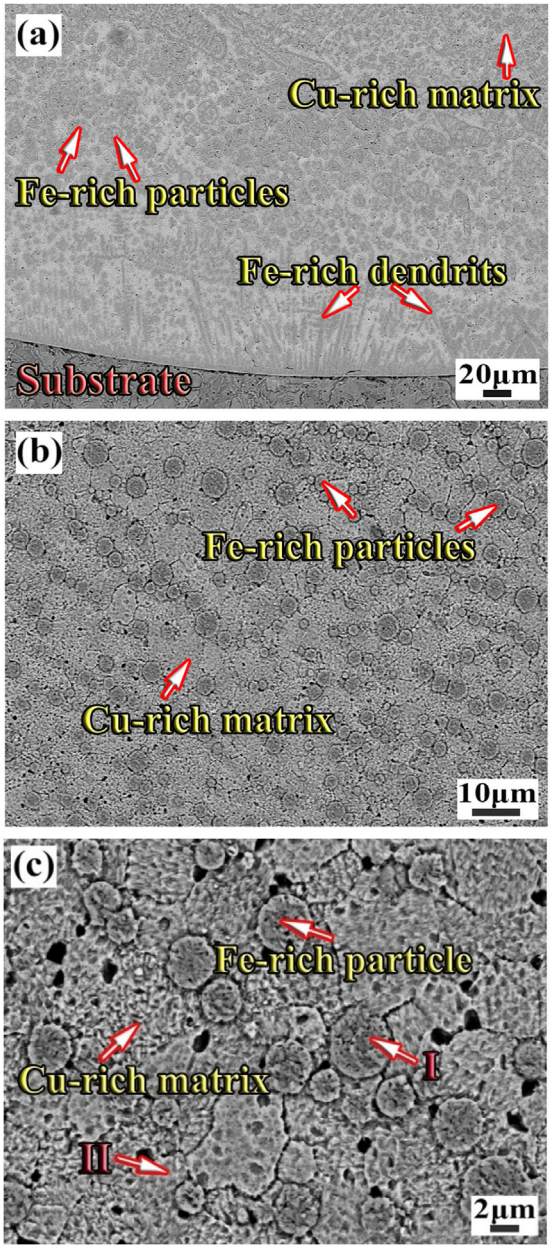

Fig. 3 – SEM images of Cu88Fe12 immiscible coating: (a) at the bottom of the coating, (b) Fe-rich particles in the Cu-rich matrix, (c) magnified image of (b).

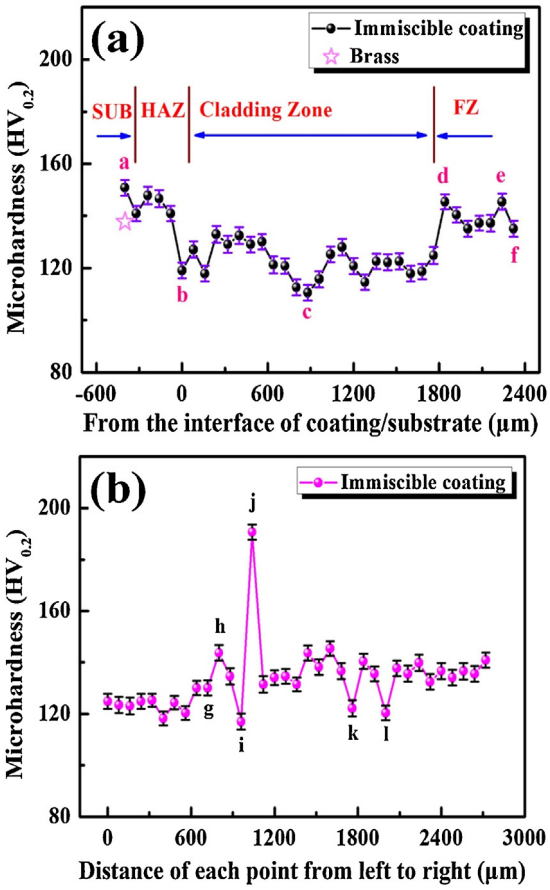

Fig. 4 – (a) Microhardness distribution along the cross-section of Cu88Fe12 immiscible coating, (b) microhardness distribution of a line which is at a distance of 2 mm from the interface of coating/substrate.

Table 2 – The EDS results on the worn surface of the immiscible coating and brass shown in Fig. 7.

Microstructure	Composition (wt.%)		
	Cu	Fe	O
III	32.0	65.8	2.2
IV	20.5	78.6	0.9
V	45.6	51.5	2.9
VI	42.1	52.5	5.4
VII	87.9	11.0	1.1
VIII	100	–	–

shows a typical cross-sectional morphologies of the immiscible coating. The planar growth with a thickness of ~3 μm is observed, suggesting that a good metallurgical bonding is formed at the coating-substrate interface. As the distance from the interface increases, the microstructure consists of fine dendrites in the metallic matrix. However, unlike the dendrites near the interface, the microstructure characteristics in the cladding zone consist of many spherical particles embedded within the metallic matrix, indicating that a typical liquid phase separation occurs as reported in literatures [23,26]. With further increase in the distance from the interface, the phenomenon of liquid phase separation is more and more remarkable so that a large amount of spherical particles with a diameter of ~4 um are homogeneously distributed in the metallic matrix (Fig. 3b and c). Moreover, the size of spherical particles has an increasing trend and the distribution density becomes higher from the bottom to the top of the immiscible coating, which can be confirmed by Figs. 4 and 5 in Section 3.2. As a result, the larger spherical particles are susceptible to be distributed on the top of the immiscible coating. Further analysis of the EDS results (Table 1) indicates that the spherical particles are rich in Fe and contain a supersaturated Cu (16.8 wt.%), whereas the metallic matrix is rich in Cu and contains a supersaturated Fe (9.1 wt.%). Additionally, the

results of XRD combined with EDS indicate that the spherical particles and the metallic matrix are γ/α-Fe and ε-Cu phases, respectively. Therefore, the microstructure characteristics of homogeneous Cu88Fe12 immiscible coating is composed of fcc γ-Fe/bcc α-Fe and fcc ε-Cu phases.

In general, laser cladding is a rapid solidification process whose cooling rate can be up to 10^6–10^7 K/s [2] and it easily results in metastable liquid phase separation in Cu–Fe binary system. When the Cu–Fe binary system is supercooled below a certain separation temperature (T_{sep}), the melt becomes metastable and spontaneously separates into two melts: Fe-rich melt L_1 (minor phase) and Cu-rich melt L_2 (major phase). Due to the combination effect of interface tension and minimum interfacial energy, the L_1 can shrink spontaneously into a large amount of small spherical liquid droplets and solidify rapidly to form the Fe-rich spherical particles, as shown in Fig. 3b and c. Furthermore, some larger spherical Fe-rich particles are observed at the top of the immiscible coating, which can be attributed to the effects of Marangoni motion due to the temperature gradient and surface tension gradient, and Stokes motion caused by the gravity field [19]. The Stokes and Marangoni motion velocities of spherical liquid droplets can be described as follows [19]:

$$V_m = \frac{-2r}{3(3u_1 + 2u_2)} \frac{\partial \sigma}{\partial T} \frac{\partial T}{\partial Z} \quad (1)$$

$$V_s = \frac{2g\Delta\rho r^2(u_1 + u_2)}{3u_2(3u_1 + 2u_2)} \quad (2)$$

where V_m and V_s are the managonic motion velocity and the Stokes motion velocity, respectively, r is the radius of Fe-rich liquid droplet, u_1 and u_2 are the viscosities of Fe-rich liquid droplet and Cu-rich matrix liquid, respectively, $\frac{\partial \sigma}{\partial T}$ is a function of the interfacial energy gradient with the temperature variation, $\frac{\partial T}{\partial z}$ is the temperature gradient, g is the gravity coefficient ($g = 9.8\,m/s^2$), $\Delta\rho$ is the density difference between Fe-rich liquid droplet and Cu-rich matrix liquid. Because the density of Fe-rich liquid droplet (L_1) is lower than the Cu-rich melt (L_2), the Fe-rich liquid droplet can keep upward movement under the action of Stokes and Marangoni motions. Meanwhile, the neighboring Fe-rich liquid droplets can attract each other by gradient-induced-coupling mechanism [13,27], due to different droplet sizes and ingredient concentrations, resulting in rapid growth of Fe-rich liquid droplets. According to Eq. (1), the larger the radius of the Fe-rich liquid droplet is, the higher the velocity of Marangoni motion (V_m) is. Thus, larger Fe-rich liquid droplet moves toward the upper zone of the molten pool. Subsequently, larger Fe-rich liquid droplets and large amounts of smaller droplets which are not swallowed by larger droplets can be encapsulated by the Cu-rich matrix during rapid solidification [26,28]. As a result, large amounts of γ/α-Fe particles with different sizes are dispersedly distributed in the Cu-rich matrix (Fig. 3).

3.2. Microhardness and wear resistance of immiscible coating

3.2.1. Microhardness characteristics

Fig. 4 shows the microhardness of different zones including substrate (SUB), heat-affected-zone (HAZ), cladding zone (CZ) and Fe-rich zone (FZ). The microhardness of the CZ exhibits an homogeneous distribution. Especially, the microhardness exhibits a significant increase at a distance of ~2 mm from the coating-substrate interface, then tends to stable at a value of $\sim 140 \pm 6.90$ $HV_{0.2}$, which is close to that of the SUB ($\sim 145 \pm 7.25$ $HV_{0.2}$). Apparently, the microhardness of the immiscible coating is higher than that of brass (138 ± 6.70 $HV_{0.2}$). The maximum microhardness at a distance of 2–3 mm from the coating-substrate interface is $\sim 191 \pm 9.55$ $HV_{0.2}$, indicating that the immiscible coating is strengthened significantly. This is attributed to the fact that large amounts of spherical Fe-rich particles dispersed within the Cu-rich matrix can result in dispersion-strengthening effect.

To further verify the result, the microscopic images of indentations corresponding to the positions in Fig. 4 under a constant load are presented in Fig. 5. The microhardness of the position a in the SUB is $\sim 150 \pm 7.6$ $HV_{0.2}$ (Fig. 4a). The low hardness of the point b or c in the CZ is due to the low distribution density of Fe-rich particles (Fig. 5), which can be considered as the hardness of the Cu-rich matrix. At the same indentation load, the sizes of microscopic indentations are diverse at the different points. By comparison, the smaller the size of microscopic indentation is, such as positions d–f, the higher the microhardness value is. The points g-l are also surrounded by Fe-rich particles (Fig. 5), especially the point j, the microscopic indentation is absolutely embedded in a large Fe-rich particle whose microhardness can reach $\sim 191 \pm 9.55$ $HV_{0.2}$, which can be regarded as the microhardness of Fe-rich particle (Fig. 5). Therefore, the existence of many Fe-rich particles can remarkably strengthen the Cu-rich matrix, and further enhancing the microhardness of the immiscible coating. In addition, the supersaturated Fe (9.1 wt.%) dissolved in the Cu-rich matrix can play an important role in solution strengthening. Therefore, the microhardness of the immiscible coating is enhanced. Particularly, the Fe-rich zone has much higher microhardness than brass.

3.2.2. Wear resistance

Fig. 6a shows the friction coefficient of Cu88Fe12 immiscible coating and Brass. At the initial stage of the dry sliding wear, the friction coefficient exhibits an unstable fluctuation that is accompanied with a sharp decline both for the immiscible coating and brass, which can be called running-in wear due to incomplete occlusal between the specimen and the ring. Apparently, the friction coefficient of the immiscible coating is larger than that of brass, showing that the increase of friction coefficient caused by the presence of many Fe-rich particles. This is because, as presented in Figs. 4 and 5, the hardness of the Fe-rich particle is significantly higher than that of the Cu-rich matrix. On the other hand, the Fe-rich particles are not easily pulled out from the Cu-rich matrix so that the motion

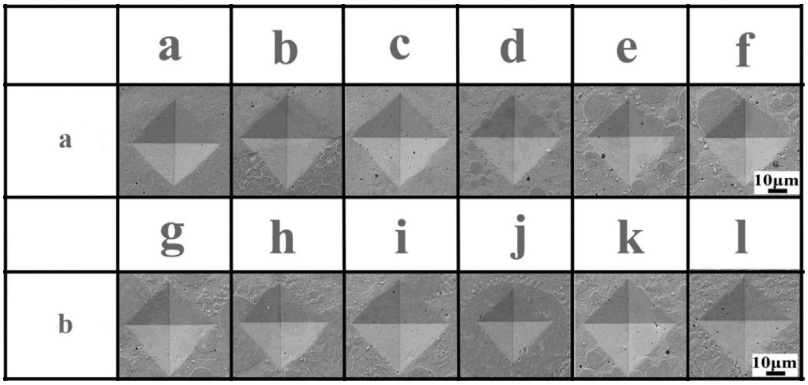

Fig. 5 – SEM images of indentation of a vertical line from substrate to coating and a horizontal line which is at a distance of 2 mm from the interface of coating/substrate as shown in Fig. 4.

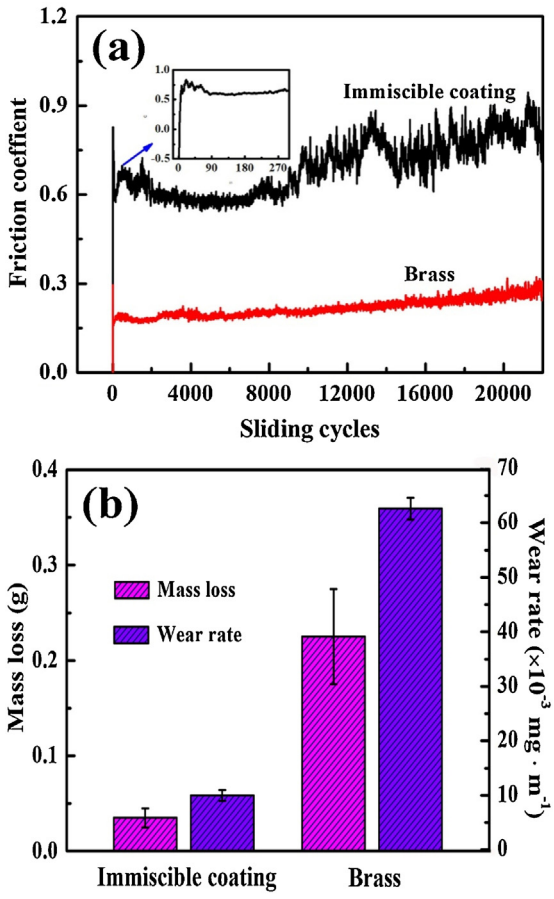

Fig. 6 – (a) Friction coefficient of Cu88Fe12 immiscible coating and brass, (b) mass loss and wear rate of Cu88Fe12 immiscible coating and brass.

resistance between the friction pairs can be increased [29–31]. Therefore, the friction coefficient of the immiscible coating is enhanced. Moreover, as seen in Fig. 6b, the mass loss of brass is 0.225 ± 0.011 g, which is approximately six times that of the immiscible coating (only 0.035 ± 0.002 g). In general, the wear rate is defined as the mass loss of the worn material per unit of the sliding distance and per unit of the constant normal load on the contact [32]. As such, the result of the wear rate (Fig. 6b) indicates that the wear resistance of the immiscible coating is significantly improved comparing with brass, which is consistent with the results of the mass loss.

Table 3 – The EDS results of wear debris from the immiscible coating and brass shown in Fig. 8.

Microstructure	Composition (wt.%)		
	Cu	Fe	O
IX	55.9	18.6	25.5
X	37.1	62.9	–
XI	100	–	–
XII	100	–	–

Fig. 7 shows the worn surface of the Cu88Fe12 immiscible coating and brass. It is apparent that the worn morphologies are characterized by plastic deformation and ploughing. The average width of ploughing on the surface of the immiscible coating (~48 ± 2.40 um) is much smaller than that of ploughing on the surface of brass (~80 ± 4.10 um) (Fig. 7a and e), suggesting that the wear degree of the immiscible coating is significantly lower than that of brass. Fig. 7b shows the ploughings and debris on the worn surface of the immiscible coating. According to the EDS analysis of marked A and B (magnified images in Fig. 7c and d) listed in Table 2, the content of Fe in the debris is much higher than the content of Cu in the debris. This suggests that the debris (III–VI) is probably Fe-rich particles which are peeled from the Cu-rich matrix (VII) and trapped on the worn surface of the immiscible coating. Additionally, the existence of O indicates that oxidation wear takes place during dry sliding wear. Comparing with the worn surface of the immiscible coating, large adhesion can be observed on the worn surface of brass (Fig. 7f) and contains only Cu (Table 2), indicating that brass suffers from significant adhesive wear during dry sliding wear.

The morphologies of the wear debris peeled from Cu88Fe12 immiscible coating and brass during dry sliding wear is shown in Fig. 8. Materials removal is in the form of slices and the fractured debris are observed due to the extrusion effect of the friction pair on the detained debris between the specimen and the counterpart ring [33,34]. The breakage of the wear debris from the immiscible coating and brass (Fig. 8a and c) are also

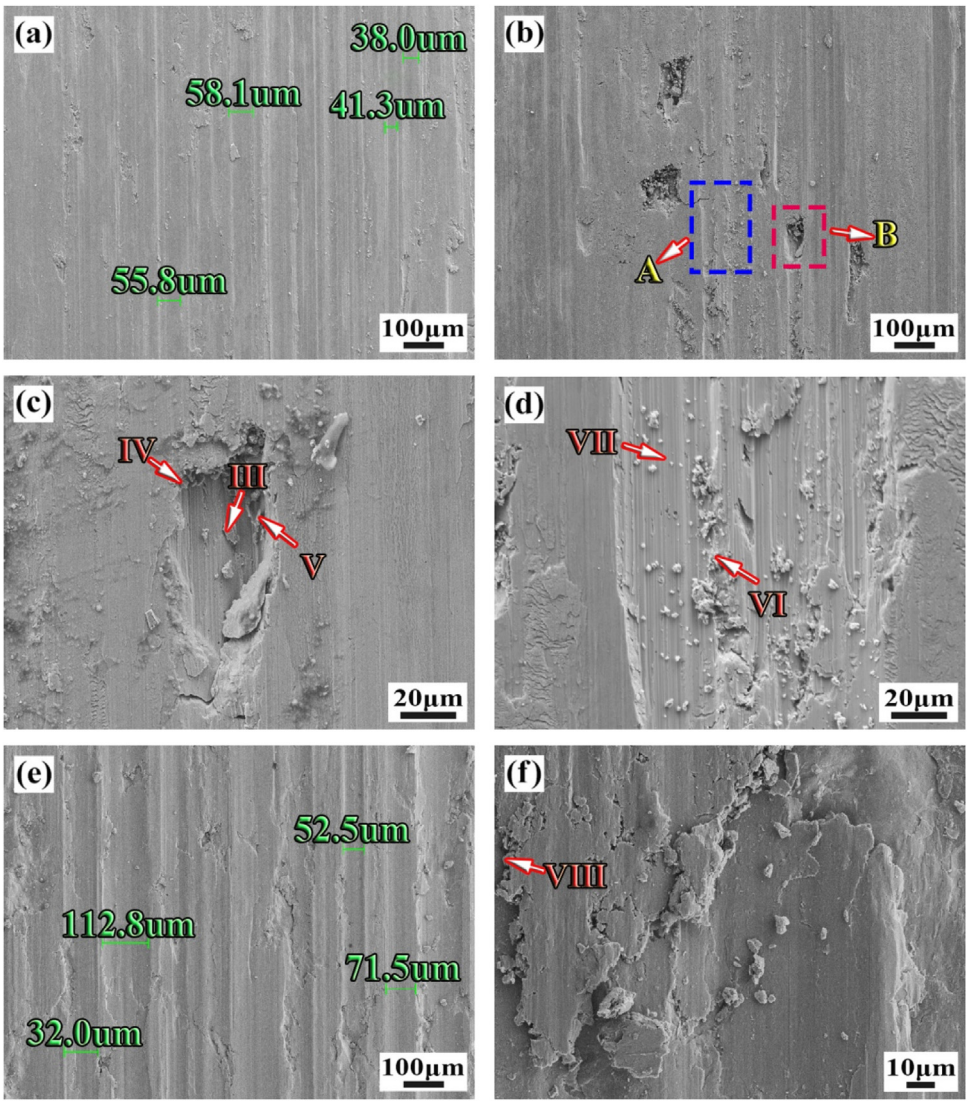

Fig. 7 – SEM images showing the morphology: (a) the ploughs on the worn surface, (b) the local spalling pits and ploughs on the worn surface, (c) magnified image of region A and (d) region B in (b) for the Cu88Fe12 immiscible coating, (e) the ploughs on the worn surface and (f) spallings of brass.

observed. According to the EDS analysis (Table 3), the lamellar debris (marked IX) from the immiscible coating are rich in Cu and a large amounts of O and Fe. This indicates that oxidation wear occurs during dry sliding wear. Moreover, many grooves, micro-cracks and fine particles are also observed on the surface of the wear debris from the immiscible coating (Fig. 8b) due to micro-ploughing caused by Fe-rich particles [35,36]. However, the wear debris from brass is only composed of the lamellar Cu metal. Comparing with the wear debris from the immiscible coating, those of brass exhibit relative smooth surface and slight crack, as shown in Fig. 8d.

The schematic diagram of immiscible coating during dry sliding wear is shown in Fig. 9. At the initial stage, the block/ring counter surfaces exhibit asperity to asperity contact. These asperities are quite sharp and are in relative motion against each other [33]. The high-hardness ring (60 HRC) leads to high stress on the surface of the immiscible coating and is accompanied with micro-cutting and micro-plowing action [37]. As a result, the Cu-rich matrix in the lamellar form is removed from the surface of the immiscible coating due to adhesive wear, as shown in Fig. 9a. Subsequently, the Fe-rich particles are protruded from the Cu-rich matrix, then the contact between the block/ring can be considered as the Fe-rich particles to the ring. These Fe-rich particles are worn preferentially to protect the soft Cu-rich matrix from direct contact with the surface of the ring. This can play a significant role in protecting the Cu-rich matrix due to "shadow protection effect" of Fe-rich particles [36], thus limiting the severe deformation and resisting the grinding and micro-cutting of the ring on the surface of the immiscible coating, resulting in the case of Fig. 9b. As a result, the depth and width ($\sim 133 \pm 6.65$ μm and $\sim 2.89 \pm 0.145$ mm) of the wear scar on the surface of the immiscible coating are less than those of brass ($\sim 175 \pm 8.75$ μm and $\sim 1.96 \pm 0.098$ mm), as shown in Fig. 10, further confirming that the immiscible coating exhibits much higher wear resistance in comparison with brass.

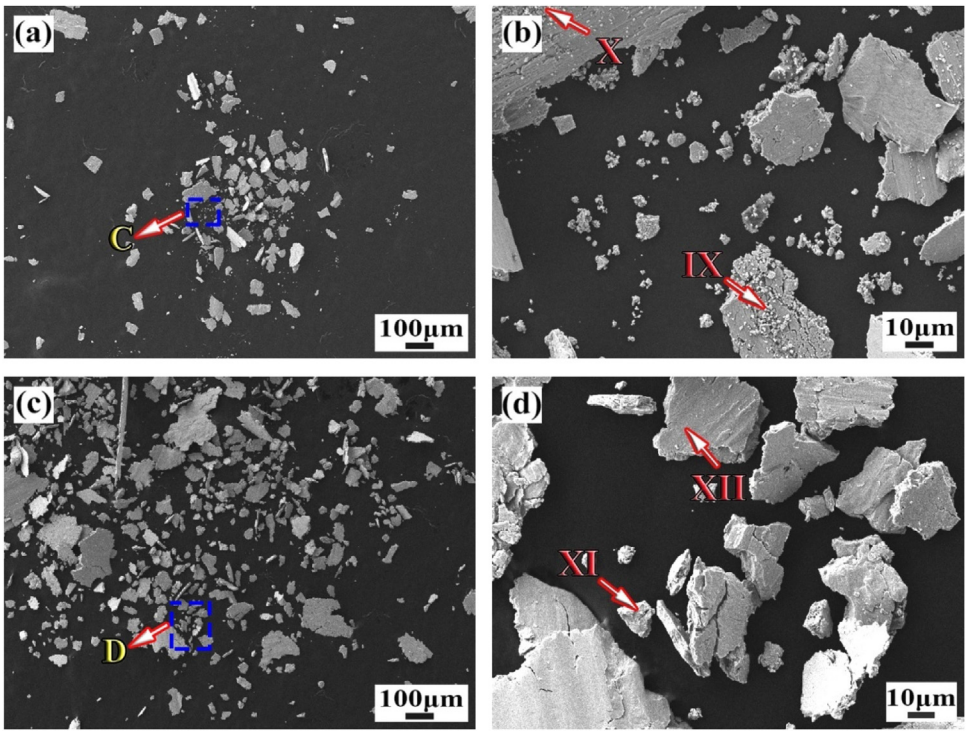

Fig. 8 – (a) Morphology of the debris from Cu88Fe12 immiscible coating, (b) magnified image of the mark C in (a), (c) morphology of the debris from brass, (d) magnified image of the mark D in (c).

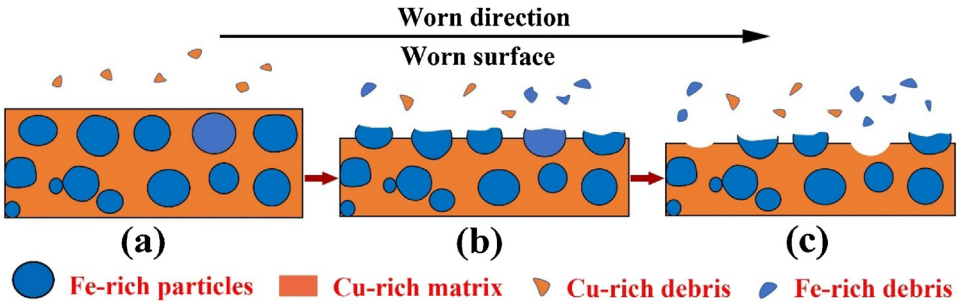

Fig. 9 – Schematic diagrams of Cu88Fe12 immiscible coating during the dry sliding wear test: (a) preferential wear of Cu-rich matrix, (b) shadow protection effect of Fe-rich particles on the Cu-rich matrix, (c) fracturing of Fe-rich particles.

With the prolonged dry sliding wear, the bonding between the Fe-rich particles and the Cu-rich matrix can be weakened due to squeezing action of counterpart ring. Once the Fe-rich particles are fractured, they can be extracted easily from the Cu-rich matrix, resulting in local spalling, as shown in Fig. 7b and c [32]. The protruding Fe-rich particles along with the Cu-rich matrix are peeled from the worn surface of the immiscible coating (Fig. 9c). Some are collected as debris (marked X in Fig. 8b) which contains a large amount of Fe and a small amount of Cu (Table 3), others are stranded on the coating/ring friction pair as the abrasive to grind on the worn surface of the immiscible coating, leading to deep ploughings by severe local plastic deformation (Fig. 7b and d) and to material loss. This results in abrasive wear of the immiscible coating. With the further prolonged dry sliding wear, the high friction resistance between the block/ring can result in temperature rise [33], which can soften the surface of the immiscible coating and decrease the mechanical engagement force between friction pair [31]. Furthermore, iron can react with oxygen to produce a smooth oxide film which not only reduces the contact area between the coating/ring friction pair, but also relieves their coarseness degree, resulting in oxidation wear. As a result, the wear mechanism of the immiscible coating is the combination of adhesive wear, abrasive wear and oxidation wear during dry sliding wear.

By comparison, the texture of brass is much softer than that of the high-hardness ring. Thus the ring can grind and cut deeply into the surface of brass, resulting in relative severe plastic deformation on the surface of brass and in large amounts of brass debris (Fig. 8c and d). Although there exists material transfer, the debris from brass is much more than that from the ring. As a result, a large amount of brass debris

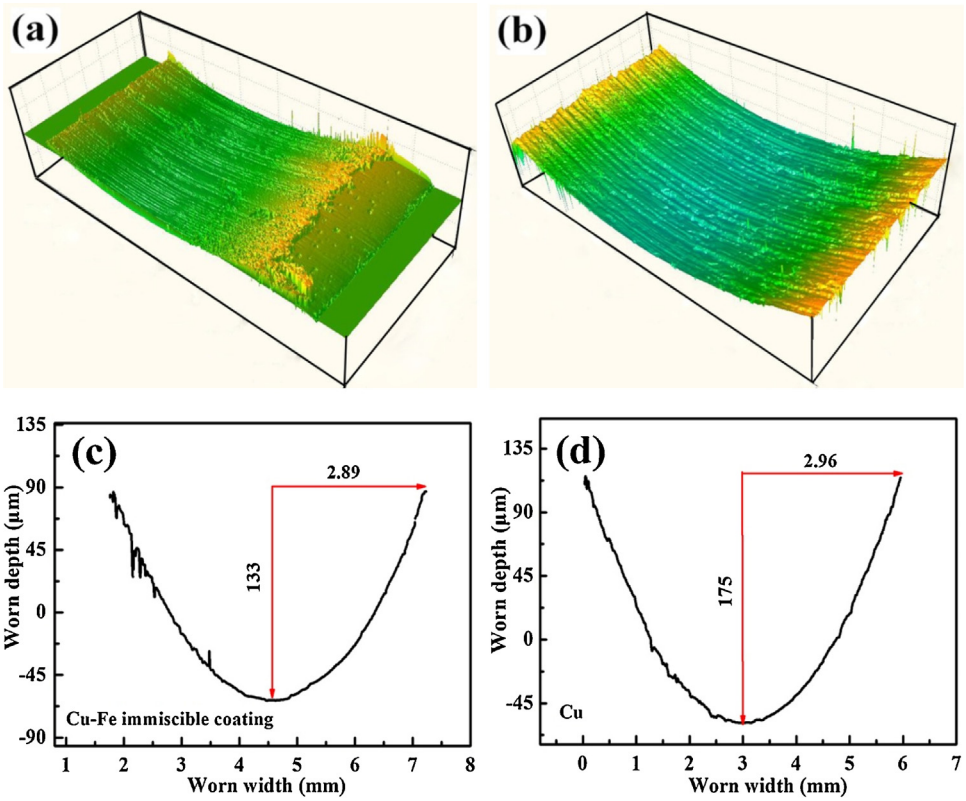

Fig. 10 – Three-dimensional images of a wear scar of (a) Cu88Fe12 immiscible coating and (b) brass, cross-section of a wear scar of (c) Cu–Fe immiscible coating and (d) brass.

can be adhered on the surface of brass (Fig. 7e and f) [30]. The contact of brass to ring (hardened GCr15 steel) is changed into brass to brass during dry sliding wear. However, the retention of brass debris between brass and ring friction pair is so short that the contact of brass to brass is immediately changed into the contact of brass to ring, leading to a slow change in friction coefficient of brass (Fig. 6a). As a result, the lamellar brass debris is peeled continuously from the worn surface of brass, whose wear mechanism are mainly characterized by adhesion wear [38].

4. Conclusions

(1) The Cu88Fe12 immiscible coating is prepared by laser cladding and the delamination phenomenon disappears. The microstructure is characterized by a large amount of spherical γ/α-Fe particles distributed homogeneously in the ε-Cu matrix. The size and distribution density of the spherical Fe-rich particles show an increasing tendency from bottom to the top of the immiscible coating.

(2) The microhardness of the Cu88Fe12 immiscible coating is enhanced due to the existence of Fe-rich particles. In particular, the hardness of Fe-rich particles in the Fe-rich zone can even reach $\sim 191 \pm 9.55$ $HV_{0.2}$, which is much higher than that of brass ($\sim 138 \pm 6.70$ $HV_{0.2}$). Moreover, the degree of plastic deformation and the width of ploughing on the worn surface of the immiscible coating are less than those of brass. As such, the wear resistance of the immiscible coating is improved remarkably comparing with brass.

(3) The wear mechanism of the immiscible coating is the combination of adhesive wear, abrasive wear and oxidation wear during dry sliding wear, while that of brass is mainly characterized by adhesion wear.

Conflicts of interest

The authors declare no conflicts of interest.

Acknowledgements

This work was financially supported by the National Natural Science Foundation of China (Grant No. 51471084) and the Outstanding Youth Foundation of Jiangxi Province (20162BCB23039), and the Natural Science Foundation of Tianjin (17JCZDJC40500), the Key Project of Department of Education of Guangdong Province (2016GCZX008), and the Project of Engineering Research Center of Foshan (20172010018).

REFERENCES

[1] Zhang K, Bian X, Li Y, Yang C, Yang H, Zhang Y. High-efficiency control of phase separation in Al-based immiscible alloys by TiC particles. J Alloys Comp 2015;639:563–70.

[2] Munitz A, Venkert A, Landau P, Kaufman MJ, Abbaschian R. Microstructure and phase selection in supercooled copper alloys exhibiting metastable liquid miscibility gaps. J Mater Sci 2012;47:7955–70.
[3] Munitz A, Abbaschian R. Liquid separation in Cu–Co and Cu–Co–Fe alloys solidified at high cooling rates. J Mater Sci 1998;33:3639–49.
[4] Munitz A. Liquid separation effects in Fe–Cu alloys solidified under different cooling rates. Metall Trans 1987;B18:565–75.
[5] Dai F, Cao C, Wei B. Phase separation and rapid solidification of liquid $Cu_{60}Fe_{30}Co_{10}$ ternary peritectic alloy. Sci China: Phys Mech Astron 2007;50:509–18.
[6] Munitz A, Bamberger M, Venkert A, Landau P, Abbaschian R. Phase selection in supercooled Cu–Nb alloys. J Mater Sci 2009;44:64–73.
[7] Elofsson V, Almyras GA, Lü B, Boyd RD, Sarakinos K. Atomic arrangement in immiscible Ag–Cu alloys synthesized far-from-equilibrium. Acta Mater 2016;110:114–21.
[8] Nagase T, Suzuki M, Tanaka T. Amorphous phase formation in Fe–Ag-based immiscible alloys. J Alloys Comp 2015;619:311–8.
[9] Hong S, Song J. Strength and conductivity of Cu–9Fe–1.2X (X = Ag or Cr) filamentary microcomposite wires. Metall Mater Trans A 2001;32:985–91.
[10] Maggio R, Ischia G, Bortolotti M, Rossi F, Molinari A. The microstructure and mechanical properties of Fe–Cu materials fabricated by pressure-less-shaping of nanocrystalline powders. J Mater Sci 2007;42:9284–92.
[11] Chen Y, Liu F, Yang G, Xu X, Zhou Y. Rapid solidification of bulk undercooled hypoperitectic Fe–Cu alloy. J Alloys Comp 2007;427:L1–5.
[12] Ma B, Li J, Xu Z, Peng Z. Fe-shell/Cu-core encapsulated metallic phase change materials prepared by aerodynamic levitation method. Appl Energy 2014;132:568–74.
[13] Shi RP, Wang CP, Wheeler D, Liu XJ, Wang Y. Formation mechanisms of self-organized core/shell and core/shell/corona microstructure in liquid droplets of immiscible alloys. Acta Mater 2013;61:1229–43.
[14] Kakisawa H, Minagawa K, Halada K. Tensile behavior change depending on the microstructure of a Fe–Cu alloy produced from rapidly solidified powder. Mater Sci Eng A 2003;340:175–80.
[15] Kobayashi A, Nagayama K. Microstructure and solidification process of Fe–Cu immiscible alloy by using containless process. J Jpn Inst Met Mater 2017;81:1–7.
[16] Wang WL, Li ZQ, Wei B. Macrosegregation pattern and microstructure feature of ternary Fe–Sn–Si immiscible alloy solidified under free fall condition. Acta Mater 2011;59:5482–93.
[17] Cao CD, Letzig T, Görler GP, Herlach DM. Liquid phase separation in undercooled Co–Cu alloys processed by electromagnetic levitation and different thermal analysis. J Alloys Comp 2011;325:113–7.
[18] Cao CD, Wei B. Disperse structures of undercooled Co–40 wt% Cu droplets processed in drop tube. J Mater Sci Lett 2002;21:341–3.
[19] Wang C, Liu X, Ohnuma I, Kainuma R, Ishida K. Formation of immiscible alloy powders with egg-type microstructure. Science 2002;297:990–3.
[20] Nagase T, Yokoyama A, Umakoshi Y. Formation of macroscopically phase separated Cu-colored melt-spun ribbon in $(Fe_{0.5}Cu_{0.5})_{100-x}B_x$ (x = 0 5, 10, and 20) alloys. J Alloys Comp 2011;509:1178–86.
[21] Zhou S, Lei J, Xiong Z, Dai X, Guo J, Gu Z. Synhthesis of Fe_p/Cu–Cu_p/Fe duplex composite coatings by laser cladding. Mater Des 2016;97:431–6.
[22] Zhou S, Wu C, Zhang T, Zhang Z. Carbon nanotube- and Fe_p-reinforced copper-matrix composites by laser induction hybrid rapid cladding. Scripta Mater 2014;76:25–8.
[23] Zhou S, Dai X, Xiong Z, Wu C, Zhang T, Zhang Z. Influence of Al addition on microstructure and properties of Cu–Fe-based coatings by laser induction hybrid rapid cladding. J Mater Res 2014;29:865–73.
[24] Dai X, Zhou S, Wang M, Lei J, Xie M, Chen H, et al. Effect of substrate types on the microstructure and properties of Cu65Fe35 composite coatings by laser induction hybrid cladding. J Alloys Comp 2017;722:173–82.
[25] Dai X, Zhou S, Wang M, Lei J, Wang C, Wang T. Microstructure evolution of phase separated Fe–Cu–Cr–C composite coatings by laser induction hybrid cladding. Surf Coat Technol 2017;324:518–25.
[26] Dai X, Xie M, Zhou S, Wang C. Formation mechanism and improved properties of Cu95Fe5 homogeneous immiscible composite coating by the combination of mechanical alloying and laser cladding. J Alloys Comp 2018;740:194–202.
[27] Tanaka H. A new coarsening mechanism of droplet spinodal decomposition. J Chem Phys 1995;103:2361–32364.
[28] Liu N, Liu F, Yang W, Chen Z, Yang G. Movement of minor phase in undercooled immiscible Fe–Co–Cu alloys. J Alloys Comp 2013;551:323–6.
[29] Xiong X, Chen J, Yao P, Li S, Huang B. Friction and wear behaviors and mechanisms of Fe and SiO_2 in Cu-based P/M friction materials. Wear 2007;262:1182–6.
[30] Zhang LC, Liu YJ, Li SJ, Hao YL. Additive manufacturing of titanium alloys by electron beam melting: a review. Adv Eng Mater 2018;20:1700842.
[31] Lei J, Shi C, Zhou S, Gu Z, Zhang L. Enhanced corrosion and wear resistance properties of carbon fiber reinforced Ni-based composite coating by laser cladding. Surf Coat Technol 2018;334:274–85.
[32] Zhou S, Lei J, Dai X, Guo J, Gu Z, Pan H. A comparative study of the structure and wear resistance of NiCrBSi/50 wt.% WC composite coatings by laser cladding and laser induction hybrid cladding. Int J Refract Met Hard Mater 2016;60:17–27.
[33] Rabadia CD, Liu YJ, Wang L, Sun H, Zhang LC. Laves phase precipitation in Ti–Zr–Fe–Cr alloys with high strength and large plasticity. Mater Des 2018;154:228–38.
[34] Zhang YS, Zhang W, Huo WT, Hu JJ, Zhang LC. Microstructure, mechanical and wear properties of core–shell structural particle reinforced Ti–O alloys. Vacuum 2017;139:44–50.
[35] Shi C, Zhou S, Dai X, Zhang LC. Microstructure and mechanical properties of carbon fibers strengthened Ni-based coatings by laser cladding: the effect of carbon fiber contents. J Alloys Comp 2018;744:146–55.
[36] Zhou S, Dai X, Zheng H. Microstructure and wear resistance of Fe-based WC coating by multi-track overlapping laser induction hybrid rapid cladding. Opt Lasers Technol 2012;44:190–7.
[37] Haque MM, Sharif A. Study on wear properties of aluminium–silicon piston alloy. J Mater Process Technol 2001;118:69–73.
[38] Shao H, Qu J. Friction and wear. Beijing: Metallurgical Industry Press; 1988. p. 120–2.